Title

Harnessing recent advances in electron cryo-microscopy single-particle analysis to improve sub-tomogram averaging

Authors

Tanmay A.M. Bharat*, Christopher J. Russo, Jan Löwe, Lori A. Passmore, Sjors H.W. Scheres*

Affiliations

Structural Studies Division, MRC Laboratory of Molecular Biology, Francis Crick Avenue, Cambridge CB2 0QH, United Kingdom

*** tbharat@mrc-lmb.cam.ac.uk and scheres@mrc-lmb.cam.ac.uk**

Summary

Recent innovations in sample preparation, data collection and image processing have led to dramatic progress in structure determination using single-particle electron cryo-microscopy (cryo-EM). In this study, we have harnessed some of these advances to improve structures determined using electron cryo-tomography (cryo-ET) and sub-tomogram averaging. We implemented a new three-dimensional model for the contrast transfer function (CTF) into the regularized likelihood optimization as implemented in the RELION program. This approach led to a sub-nanometre resolution structure of hepatitis B capsids from tomographic data collected on a direct electron detector. In addition, we used a combination of single-particle analysis and sub-tomogram averaging to analyse radiation-induced movements of the sample. In line with recent observations made in single-particle analysis, we found that significant sample movements do occur during tomographic data collection, and that reduction of these movements through the use of ultrastable gold substrates lead to further improvements in resolved details.

Introduction

High-resolution structure determination by single-particle analysis (SPA) of electron cryomicroscopy (cryo-EM) data is undergoing rapid progress. New direct electron detectors have recently yielded images of outstanding quality, with signal-to-noise ratios that are significantly better than what was previously available on film (McMullan et al., 2014; McMullan et al., 2009). Direct electron detectors also record images at high speeds, so that each exposure can be divided into multiple image frames. These direct electron detector movies can be used to correct for the image blurring caused by radiation-induced specimen movements, which results in a restoration of high-resolution features in the images (Brilot et al., 2012; Campbell et al., 2012; Fromm et al., 2014; Li et al., 2013; Scheres, 2014). Added to these hardware developments, improvements in refinement algorithms have also made image alignment and classification more accurate, resulting in higher-resolution structures from lower amounts of cryo-EM data than previously possible (Bai et al., 2013; Scheres, 2012a). This has led to an avalanche of near-atomic resolution cryo-EM structures by single-particle analysis, e.g. (Allegretti et al., 2014; Bartesaghi et al., 2014; Liao et al., 2013; Wong et al., 2014).

Single-particle analysis requires images of many identical copies of a macromolecule in different ‘views’. Each of these 'views' corresponds to a two-dimensional (2D) projection of the Coulomb potential (or cryo-EM density) in the particle of interest. In the Fourier domain, the 2D projections are central slices through the three-dimensional (3D) Fourier transform of the Coulomb potential, and the corresponding projection directions determine the orientations of these 2D slices. Each image must be aligned with respect to the 3D structure, in order to precisely orient each 2D Fourier slice. Because radiation damage puts stringent limitations on the electron dose one can use for imaging, the signal-to-noise ratio in these images is low and one needs to average over many images. With the new detectors, near-atomic resolution reconstructions now require several tens of thousands of individual particle images to be combined into one structure (Bai et al., 2013).

For many specimens, the requirement of being able to record images of individual macromolecules as separated 'views' is hard to meet because the macromolecule of interest is only ever present in a complex 3D environment. Here, other molecules surround the target macromolecule, and in 2D cryo-EM images the target signal is superimposed with the signal originating from the environment. Examples of these types of specimens include complex macromolecules like flagella (Lin et al., 2014), asymmetric viruses like HIV-1 or Herpesvirus (Briggs et al., 2009; Grünewald et al., 2003; Subramaniam, 2013), purified parts of cells like the nuclear pore complex (Beck et al., 2007) or even whole cells (Bharat et al., 2011; Tocheva et al., 2011). For these complex samples, electron cryo-tomography (cryo-ET) is an alternative method of 3D structure determination. In cryo-ET multiple low-dose 2D cryo-EM images of the specimen are collected as a tilt series, i.e. as multiple images at different tilt angles of the sample relative to the electron beam (Baumeister, 2002). These images are then used to obtain a tomogram, which is a 3D reconstruction of the entire field-of-view. Because of the geometry of specimen holders, high-tilt images cannot be recorded, resulting in an empty region in the 3D Fourier transform of a tomogram. When the sample is tilted around a single axis, this region is wedge-shaped and is often referred to as the missing wedge. Apart from specific artifacts that are caused by the missing wedge, a tomogram is an accurate representation of the

arrangement of the Coulomb potential of the specimen in 3D, and within a tomogram multiple repeating structures may be present.

Three-dimensional averaging of repeating structures in tomograms, or sub-tomogram averaging (STA), may further reduce noise and thus reveal higher-resolution information about those structures (Bartesaghi and Subramaniam, 2009; Briggs, 2013; Förster et al., 2005). Recent progress in cryo-ET data collection schemes with improved defocus stability over the entire tilt series, and new image processing algorithms with contrast transfer function (CTF) correction have allowed sub-nanometre resolution structures to be determined using sub-tomogram averaging (Schur et al., 2014). In addition, hybrid image processing approaches have been described that use information from sub-tomogram averaging to guide single-particle analysis (Bartesaghi et al., 2012; Bharat et al., 2014; Bharat et al., 2012). Still, the highest resolution structures obtained in sub-tomogram averaging are significantly lower in resolution than those obtained recently by single-particle analysis, and it is not entirely clear why this is the case.

Multiple tilt-series images need to be recorded to adequately sample the 3D Fourier space during tomographic data collection. Since radiation damage limits the total electron dose that can be applied to the specimen, each image of the tilt series is typically collected with a fraction of the dose applied in conventional single-particle cryo-EM images (1-5 $e^-/Å^2$ vs. 25-30 $e^-/Å^2$). It is therefore more difficult to accurately estimate CTF parameters in tomography, particularly from high-tilt images where the effective signal-to-noise ratio is very low (Eibauer et al., 2012). Overall however, typical electron doses applied over the entire tilt-series (40-100 $e^-/Å^2$) are higher than in conventional single-particle analysis (25-30 $e^-/Å^2$). This extra electron dose destroys high-resolution features in the specimen, and ultimately limits the attainable resolution in sub-tomogram averaging. Apart from these limits imposed by radiation damage, it could also be that the algorithms used for sub-tomogram averaging align and classify the individual particles less accurately than analogous single-particle analysis algorithms. Furthermore, it can be expected by extrapolation from experience in single-particle analysis that radiation-induced motion of the specimen is likely also a factor limiting tomogram quality (Brilot et al., 2012; Campbell et al., 2012; Rubinstein and Brubaker, 2014).

In this study we sought to use recent advances in single-particle analysis to improve sub-tomogram averaging. The (empirical) Bayesian approach to image processing in the RELION program (Scheres, 2012a, b), which has proven powerful for classification and high-resolution refinement of single-particle data (Bai et al., 2015), was extended for sub-tomogram averaging refinement. A new 3D CTF model was developed within the Bayesian framework of RELION, which allows full CTF phase and amplitude correction. The parameters for this 3D CTF model, which also compensates for the missing wedge, were estimated using an extended tilt-series data acquisition scheme on a direct electron detector. In addition, we performed experiments to show that radiation-induced specimen motion is an important limitation in tomogram quality. Thus, we used recently developed ultrastable gold substrates, which significantly reduce radiation-induced motion (Russo and Passmore, 2014) to improve tomogram quality and improve the resolution obtained using sub-tomogram averaging.

Approach

Image processing

The image processing approach to sub-tomogram averaging presented here builds directly on the (empirical) Bayesian approach to single-particle reconstruction presented previously (Scheres, 2012b; Scheres and Chen, 2012). The main differences lie in the three-dimensionality of the data, and the way the tomographic missing wedge and the CTF are treated simultaneously. As before, the data model is formulated in the Fourier domain:

$$X_i = \mathrm{CTF3D}_i \mathbf{R}_{\phi_i} V_k + N_i, \quad (1)$$

where:

- X_i is the three-dimensional Fourier transform of the i^{th} experimental sub-tomogram, with $i=1,\ldots, N$.
- $\mathrm{CTF3D}_i$ is a three-dimensional model in the Fourier domain that describes both the effects of the objective lens' CTF on the two-dimensional images in the tilt series, and the effects of the missing wedge. This model is described in more detail below. It is an input parameter that is experimentally estimated.
- $\mathbf{R}_{\phi_i}$ is a transformation that describes a combined rotation and translation ϕ_i in the real domain, *i.e.* a rotation and a phase-shift in the Fourier domain.
- V_k is the 3D Fourier transform of the k^{th} of K references, or underlying structures in the data set. Values of $K > 1$ may be used to describe structural heterogeneity in the data; and K is an input parameter. All Fourier components of all K references are assumed to be independent, zero-mean, and Gaussian distributed with a variance τ_k^2 that is a function of the spatial frequency.
- N_i is noise in the three-dimensional Fourier space. For all Fourier components of all N experimental sub-tomograms, this noise is assumed to be independent, zero-mean and Gaussian distributed with variance σ_i^2 that is a function of spatial frequency.

As in the case of single-particle reconstruction, a regularized likelihood function is optimized. The likelihood of observing the data given a model comprising $\{V_k, \tau_k^2, \sigma_i^2\}$ is extended with a regularization term that imposes smoothness in the real domain, by penalizing strong high-frequency components in the Fourier transform of the references. The derivation of the expectation-maximization algorithm (Dempster et al., 1977) that optimizes the regularized likelihood function is exactly the same as for the single-particle case (Scheres, 2012b) and is not repeated here. The resulting iterative algorithm becomes:

$$V_k^{(n+1)} = \frac{\sum_{i=1}^{N} \int_{\varphi} \Gamma_{i\varphi}^{(n)} \mathbf{R}_{\varphi}^{\mathrm{T}} \frac{\mathrm{CTF3D}_i}{\sigma_i^2} X_i \, d\varphi}{\sum_{i=1}^{N} \int_{\varphi} \Gamma_{i\varphi}^{(n)} \mathbf{R}_{\varphi}^{\mathrm{T}} \frac{\mathrm{CTF3D}_i^2}{\sigma_i^2} d\varphi + \frac{1}{\tau_k^2}} \quad (2)$$

$$\sigma_i^{2(n+1)} = \frac{1}{2}\int_{\varphi} \Gamma_{i\varphi}^{(n)} \left\| X_i - \mathrm{CTF3}D_i \mathbf{R}_{\varphi} V_k^{(n)} \right\|^2 d\varphi \quad (3)$$

$$\tau_k^{2(n+1)} = \frac{1}{2}\left\| V_k^{(n)} \right\|^2 \quad (4)$$

where *(n)* is the iteration number, and $\Gamma_{ik\phi}^{(n)}$ is the posterior probability of class assignment *k* and orientation assignment ϕ for the i^{th} sub-tomogram.

In the single-particle approach, the iterative algorithm is started by providing a single reference structure. In the test case presented in this study, the initial reference could also be generated *de novo* from the data itself by starting from random orientational assignments for all sub-tomograms. If K > 1, then multiple starting models are generated by random division of the data set in the first iteration. Initial estimates for τ_k^2 and σ_i^2 are calculated from power spectra of the initial reference and the experimental sub-tomograms, respectively.

This approach to sub-tomogram averaging was implemented in the open-source RELION program (Scheres, 2012b), and will be distributed freely in the 1.4 release. By re-using the existing implementation for single-particle analysis, the resulting program conveniently taps into a range of developments for single-particle analysis. This provides direct access to the automated refinement procedure in RELION (called 3D auto-refine in RELION), which includes a procedure to estimate angular accuracies (Scheres, 2012b), and employs a "gold-standard" procedure for refinement of two independent half-sets (Scheres and Chen, 2012) . Also the post-processing functions in RELION are directly applicable. These include auto-masking functionality, a procedure to estimate the effects of masking on the FSC (Chen et al., 2013), and automated B-factor correction for those cases that extend significantly beyond 10 Å resolution (Rosenthal and Henderson, 2003). In addition, the particle extraction and normalization functionality of RELION was expanded to include 3D data, in order to facilitate entry into the RELION workflow starting from (x,y,z) coordinates (in the RELION-specific STAR format or in flat ASCII) and tomograms in the MRC format.

CTF model

The aberrations of the objective lens of the microscope and the effects of taking images underfocus, which are approximated in the Fourier domain by the CTF, affect the 2D images that form the tilt series of a tomography experiment. Therefore, the three-dimensional $\mathrm{CTF3D}_i$ model described above is somewhat artificial. $\mathrm{CTF3D}_i$ is obtained by calculating 2D CTFs of all the images in the tilt series, and placing them as central slices into a three-dimensional Fourier transform, where the orientation of the slices is determined by the tilt angles of the images in the series. For this, we use a modification of the reconstruction algorithm in the RELION package (Scheres, 2012b). Figure 1A-B shows the result for a typical $\mathrm{CTF3D}_i$. This function not only expresses information about the CTF modulations for each of the images in the tilt series (which as explained in the next section may be estimated as a function of the position of each particle in the tomogram). It also expresses information about the

sampling of the tilt angle and (thus) the extent of the missing wedge. Thereby, one could interpret $\mathrm{CTF3D}_i$ as a function that describes the information transfer from a true molecular structure inside the microscope to each of the individual 3D Fourier components of the i^{th} experimental sub-tomogram.

In the current implementation, generation of all $\mathrm{CTF3D}_i$ is performed using customized python scripts that are outside the RELION workflow, although these scripts do use the stand-alone reconstruction program in RELION (relion_reconstruct). These scripts may be downloaded from the RELION wiki pages (http://www.mrc-lmb.cam.ac.uk/relion).

CTF estimation and weighting

The new CTF model requires defocus estimates for each particle in all images of the tilt series. For this, we used an extended tilt series acquisition scheme (Eibauer et al., 2012) implemented in SerialEM (Mastronarde, 2005). Tomographic data was acquired on a direct electron K2-summit detector fitted behind a Gatan Quantum energy filter. Two additional, high-dose images were collected on either side of the region of interest along the tilt axis at the same distance (Figure 1C). The average defocus of each extra image was estimated using CTFFIND3 (Mindell and Grigorieff, 2003). The arithmetic mean of the estimated defoci for both extra images at each tilt was found to be a good estimate for the actual defocus value for the tilt series image (Figure 1D). Thus, this extended tilt series acquisition scheme provided CTF parameters for all images of the tilt series.

Sub-tomograms extracted from different parts of the image have a different defocus due to the tilting of the grid. Based on the position of the sub-tomogram in the reconstructed tomogram, we calculated the height difference of each particle in each image of the tilt series relative to the tilt axis. Adding the height difference to the average defocus of the tilt series image (calculated above) provided a local estimate of defocus for each sub-tomogram in each image of the tilt series.

Next, we sought to use the CTF model to appropriately weight the information present in the tilt series data. The effective thickness of the specimen increases at increasing tilt angle by a factor of the cosine of the tilt angle. We postulated that the signal-to-noise in the tilted images decreases proportionally to the increasing ice thickness. Thus, the 2D CTF function in slices corresponding to each tilted image in the 3D CTF model were damped down uniformly at all resolutions by multiplication with a factor equal to the cosine of the tilt angle (Figure 1E).

During data acquisition, the biological specimen is damaged by accumulated radiation. Based on early reports on radiation damage (Downing, 1988; Henderson and Glaeser, 1985; Wright et al., 2006), we assumed that the higher resolution Fourier components are destroyed first, and used a recently introduced radiation damage model for single-particle analysis (Scheres, 2014) to describe the fall-off of signal in the tilt series. We applied a dose-dependent B-factor to dampen the high-frequency components of images that were recorded later in the tilt series. Based on observed B-factors for single-particle analysis (Scheres, 2014), we chose to use a linear increase of 4 Å^2 in the B-factor with each electron per Å^2 of accumulated electron dose (Figure 1F). The combined tilt angle-dependent scale factor and the dose-dependent B-factor were used to get the final weighted CTF model (Figure 1G-H).

Limiting radiation-induced motion with data collection on gold grids

Radiation-induced movement of the specimen is known to limit resolution in single-particle analysis. In single-particle analysis, loss in resolution for each exposure due to radiation-induced motion can be prevented using movie-processing algorithms, either by re-aligning entire micrographs (Li et al., 2013) or on a per-particle basis (Brilot et al., 2012; Scheres, 2014). For tomography, data are acquired in a different way. Instead of one single exposure, the sample is irradiated multiple times in short pulses at different tilt angles of the specimen. The applied electron dose at each tilt angle can be fractionated in a movie, which can be used to compensate for radiation-induced motion within each of the short exposures. However, correcting for specimen movement that occur from one tilted image to the next is not straightforward. For this reason, in sub-tomogram averaging one cannot use per-particle movie-processing to recover the high-resolution signal as one would do in single-particle analysis. To study the effect of the beam on the specimen in tomography, tilt series data were collected on a DNA-origami test specimen (discussed below) and changes in the specimen that occured during data acquisition were analyzed.

To preserve high-resolution information in tomography better, we used specimen supports that reduced radiation-induced motion of the specimen. Ultrastable specimen supports made entirely of gold have been shown to do this in single-particle analysis (Russo and Passmore, 2014). The same ultra-stable gold substrates were used in this study for tomography. These were specially optimized so that the size of the hole containing vitreous ice was roughly the same as the field of view in the untilted image of the tilt series. Since 10 nm gold fiducials are not easy to spot and track on a substrate that is itself made of gold, the concentration of fiducials was optimized to yield 8-12 markers in each hole.

During data collection, the hole was illuminated symmetrically with the centre of the beam coinciding with the centre of the hole. Since the gold support is a very high intensity feature, it can be seen at extremely low electron doses. Therefore, a low-dose image (0.05 $e^-/Å^2$) was collected prior to tilt series data collection. Using this image, the hole was centered using image shift before commencing data collection. Finally, because only the specimen embedded in vitreous ice and not the gold grids show Thon rings (in Fourier transforms of images), the extra images for defocus estimation (*cf.* Figure 1C) were positioned so that they illuminated holes on either side of the region of interest.

Results

Hepatitis B capsid as a test sample

We selected the hepatitis B virus (HBV) capsid protein as a test sample for our sub-tomogram averaging approach. This protein forms a closed protein shell with icosahedral symmetry. The X-ray structure of this capsid is known (Wynne et al., 1999), which allows straightforward assessment of sub-tomogram reconstruction quality.

We collected cryo-ET data on this sample (Figure 2A) and reconstructed tomograms from the data (Figure 2B). Tilt series alignment based on the gold fiducials was performed in IMOD, and the actual tomogram reconstruction was performed using weighted-back projection in Tomo3D (Agulleiro and Fernandez, 2011). Particles were extracted from the reconstructed tomograms using the template matching algorithm in the MolMatch software (Förster et al., 2005). To remove

extracted sub-tomograms that did not correspond to HBV capsids we conducted reference-free classification of the tomograms in the initial data set, using K=2 in Equations 1-2 (Figure S1A-B). This classification readily allowed identification of real HBV capsid particles from the false positives that corresponded to 10 nm gold fiducials. We found that another efficient way to achieve a similar result is to project each sub-tomogram into a 2D image along the direction of the electron beam (Figure S1C), and to conduct reference-free classification of these 2D projections just like one would perform 2D class averaging in single-particle analysis. This has been implemented as an easily accessible option in the particle extraction program of RELION. We propose that 2D classification of projected sub-tomograms could be a fast and efficient way to detect good particles in sub-tomogram averaging.

For initial refinement tests with the identified HBV sub-tomograms, we used a 50 Å low-pass filtered version of the X-ray structure as a starting model. To investigate the effects of our new CTF model, we first conducted a refinement of the extracted particles without any CTF correction (Figure 2C). This refinement did not yield a high-resolution structure, and the final volume had no distinct features. Next, we conducted a refinement with the same parameters, with the unweighted 3D CTF model applied (see Figure 1A-B). In this case, a 10.2 Å resolution structure was obtained (Figure 2D) showing that the 3D CTF model in our algorithm was a good approximation for the actual CTF of the microscope during data collection. Use of the tilt-angle and electron-dose weighted 3D CTF model (Figure 1G-H) led to a further improvement in resolution to 9.2 Å (Figure 2E-G). Clear rod-shaped densities for α-helices in the map confirmed the estimated resolution (Figure 2H).

To compare our new 3D CTF model with traditional strip-based CTF correction schemes, we conducted the same refinement with data extracted from tomograms that had been CTF corrected in IMOD using strip-based phase-flipping (Kremer et al., 1996). The obtained resolution (10.9 Å) was lower, even compared to using the 3D CTF model without the tilt-angle and radiation damage weighting, showing that our new CTF model more accurately compensates for the CTF of the microscope (Figure S2A-B). The resolution of the highest-resolution sub-tomogram averaging structure (9.2 Å) could not be improved by the addition of more data, or by removing subsets of the data with the highest dose (Figure S3).

Even though a low-pass filtered X-ray model was used for the above tests, a starting model could also be obtained from the data itself by starting refinement from randomly assigned orientations to all sub-tomograms (Figure S2C-D). The resulting model was of a slightly lower quality (11.5 Å) than the one obtained above, but using this as a starting model for a second refinement led to the same resolution as in the tests with an externally provided initial model.

Comparison of sub-tomogram averaging and single-particle analysis on the same sample

Our best resolved sub-tomogram averaging map (9.2 Å) remained far from limits imposed by the Nyquist frequency (4.3 Å). As a next test, we decided to compare sub-tomogram averaging and single-particle analysis refinements for the same particles. For this, we pre-exposed the HBV capsid sample, collecting a conventional 2D cryo-EM image with a 6 $e^-/Å^2$ dose (Figure 3A), and then acquired a tilt series of the same region (Figure 3B) with a dose of 60 $e^-/Å^2$. We used the tilt series data for tomographic reconstruction and extracted 1501 HBV sub-tomograms for sub-

tomogram averaging. The same particles were also selected from the pre-illuminated images for conventional single-particle analysis refinement. Sub-tomogram averaging produced a map at 10.5 Å resolution (Figure 3C, blue curve), while single-particle analysis refinement yielded a 6.1 Å resolution map (Figure 3C, purple curve).

Although the accumulated radiation damage in the pre-illuminated images is lower than in the tomographic tilt series, the difference in resolution seemed larger than expected from radiation damage alone (Scheres, 2014). Indeed, cryo-EM single-particle analysis reconstructions with convincing side-chain densities have been conducted using images that were pre-irradiated with electron doses much higher than 6 $e^-/Å^2$ (Allegretti et al., 2014; Fromm et al., 2014) The unexplained difference in resolution could be either due to poor orientational assignments in the sub-tomogram averaging refinement, or due to an intrinsically lower quality of the sub-tomograms compared to the single-particle image. To test this we calculated pair-wise Euler angle differences between the two refinements for each particle (Figure S4), and divided the sub-tomograms into two subsets. Subset 1 contained half of the sub-tomograms (751 particles) that were assigned most similar angles in both sub-tomogram averaging and single-particle analysis refinements. Subset 2 contained the other half of the data set (750 particles), i.e. sub-tomograms that were aligned with the most different angles in the sub-tomogram averaging and single-particle analysis refinements. Sub-tomogram averaging refinements of these two subsets yielded maps with similar resolutions (Figure 3D), indicating that alignment quality was not the limiting factor of the sub-tomogram averaging map. To confirm this, we also calculated an average of all sub-tomograms where we assigned the angles determined in the single-particle analysis refinement. Also this reconstruction did not lead to any improvement in resolution. These results suggest that the quality of the sub-tomograms themselves is limiting the resolution of sub-tomogram averaging refinement.

Radiation-induced motion causes imperfections in tomogram reconstruction

Because radiation-induced specimen motions have been shown to have an important effect on the resolution of single-particle analysis reconstructions (Bai et al., 2013; Brilot et al., 2012; Li et al., 2013; Scheres, 2014), we decided to analyze such motions during tilt series data collection. Our aim was to independently track and orient each particle in each image of the aligned tilt series, and to compare its position and orientation to that in the final reconstructed tomogram. For these tests we selected DNA origami molecules that are specifically designed, large (6MDa), high-contrast particles with an asymmetrical shape to facilitate alignment (Bai et al., 2012). To further increase signal-to-noise ratios in the individual images, we collected tilt series at a relatively high defocus (-7 μm) and dose (70 $e^-/Å^2$), and avoided tilt angles above 30°. The alignment of the tilt series was conducted using gold fiducials as markers, and it did not rely on the DNA origami particles.

Sub-tomograms were selected manually from the tomographic reconstructions (Figure S5A), and these particles were carefully tracked to the individual particles in the aligned tilt series images (Figure S5B). Using a 11 Å resolution cryo-EM structure of this DNA origami molecule obtained previously (EMD-2210) as a reference, we assigned Euler angles and shifts to the sub-tomograms as well as the particles in each image of the tilt series. We compared the assigned Euler angles in the sub-tomogram averaging and single-particle analysis alignments in a tilt-pair-like analysis (Rosenthal and Henderson, 2003) (Figure S5C-D). In the absence of radiation-induced rotations

in the sample (and without any errors in the orientational assignments), the plot would resemble the inset in Figure S5D. We only selected particles where the plots were roughly on a line (white lines in Figure S5C-D) and our analysis showed significant departure from the ideal behavior (mean 3.8° ± 2.6° from the ideal vertical axis, Figure S5C-D). In the absence of radiation-induced specimen motion, the difference in assigned in-plane shifts between particles extracted from the aligned tilt series and the corresponding sub-tomograms should be zero. However, for the selected subset of particles we observed differences in shifts with mean 5.8 ± 4.0 Å (Figure S5E-F). These results indicate that radiation-induced sample motions do occur during acquisition of the tilt series data. These motions will violate the starting assumption of the tomographic experiment that each image in the tilt series corresponds to a projection of the same 3D structure.

Gold-grid data collection: reducing radiation-induced motion

Recently, specimen supports where both the grid and the holey film are made of gold have been shown to significantly reduce radiation-induced specimen motions (Russo and Passmore, 2014). To test the effects of these ultra-stable grids on sub-tomogram averaging, we repeated the HBV data collection as presented in Figure 2 on gold grids (Figure 4A-B).

The observation that no radiation-induced sample motions could be identified upon visual inspection of the tilt series was confirmed by analyzing the residuals between the actual and the expected position of the fiducial markers in the aligned tilt series as calculated in IMOD. Comparison of these values with those from the data collected on ordinary carbon support grids indicated that the movement of the fiducials was reduced by nearly a factor of two on the gold grids (Figure S6). The overall average residual on the gold grids was 2.3 Å (over 11 tilt series), compared to 4.3 Å (over 15 tilt series) on ordinary carbon support grids.

Application of the same sub-tomogram averaging procedure with the weighted 3D CTF model yielded a higher resolution map (8.1 Å) from fewer particles than before (1,145 instead of 1,851, Figure 4C-F), supporting the observation from the DNA origami experiment that radiation-induced motion of the specimen during tilt series acquisition is indeed preventing higher resolution refinement from cryo-ET data.

Discussion

In this study, we have developed and applied an approach to sub-tomogram averaging in which we harnessed recent developments in single-particle analysis. We extended the regularized likelihood refinement algorithm in RELION to three-dimensional images, and used ultra-stable gold grids to reduce radiation-induced sample movements. Using sub-tomogram averaging on a hepatitis-B capsid sample, we demonstrate that this approach allows sub-nanometre resolution structure determination of biological macromolecules.

The extension of the (empirical) Bayesian approach in RELION to 3D data called for a new 3D CTF model. This model expresses both phase and amplitude data for the information transfer at every point in the 3D Fourier transform of each individual sub-tomogram. Thereby, it may be used to model the missing wedge (or the geometry of the tilt series in general); variations in defocus over the tilt series; and

the loss of signal in higher-tilt images. In addition, we used knowledge about radiation-induced damage from single-particle analysis experiments to down-weight the contribution of the higher-dose images in our 3D CTF model. To our knowledge, this is the most comprehensive CTF model used in sub-tomogram averaging to date. To make full use of the new capability that this model provides for CTF correction, we used a previously described extended tilt series acquisition scheme (Eibauer et al., 2012) that allows accurate CTF estimation for all images in the tilt series, even at high tilt angles. Without CTF correction, averaging of HBV sub-tomograms resulted in a featureless structure, whereas the new model outperformed the conventional strip-based phase flipping approach as implemented in IMOD (Kremer et al., 1996), even when only correcting for the CTF, i.e. without using the tilt-angle and dose-dependent weighting scheme (*cf.* Figs 2F and S2B).

Still, our experiments with a combined approach on the same sample illustrated that single-particle analysis yields significantly higher resolutions than sub-tomogram averaging. Admittedly, recording the pre-illuminated image prior to the tilt series leads to an additional dose of 6 $e^-/Å^2$ in the latter that would not be present in a conventional tomography experiment. However, Allegretti *et al* (Allegretti et al., 2014) observed that for F_{420}-reducing [NiFe] hydrogenase, near-atomic resolution reconstructions with convincing side-chain densities could still be calculated from single-particle images that were pre-irradiated with doses much higher than 6 $e^-/Å^2$, and similar observations were made for β-galactosidase by Bartesaghi *et al* (Bartesaghi et al., 2014). Therefore, increasing the total dose in the sample after tilt series acquisition from 60 $e/Å^2$ to 66 $e/Å^2$ by pre-illuminating the sample in our experiment (while also down-weighting later images using the B-factor weighting as in Figure 1F) is not likely to explain the difference between the 10.5 Å resolution for the sub-tomogram average and the 6.1 Å resolution for the single-particle reconstruction. Comparison of the orientations assigned to the sub-tomograms and the single-particle projections, and a reconstruction from the sub-tomograms with the orientations as determined from single-particle analysis, showed that it also not likely that errors in the sub-tomogram alignment limit the resolution of the sub-tomogram averaging approach. Therefore, we hypothesize that the quality of the tomograms themselves is a limiting factor for the resolution of the sub-tomogram average, although we cannot rule out that residual errors in our CTF correction and/or radiation-damage weighting scheme also play a role.

In single-particle analysis, radiation-induced sample motion has been observed to limit resolution of the reconstruction, but movie-processing algorithms may be employed to (partially) correct for these movements (Bai et al., 2013; Brilot et al., 2012; Li et al., 2013; Scheres, 2014). Although using similar movie-processing algorithms may correct motions within each image of a tomographic tilt series, correction for sample movement from one tilted image to the next is currently not possible. In many tomography experiments, the gold fiducial markers that are used to align the tilt series have been observed to move during data acquisition. If only the fiducial markers would move but not the objects of interest, then this movement would deteriorate the tilt series alignment, but the underlying assumption of a constant 3D macromolecular or cellular structure in the field of view would still be fulfilled. In that case, provided one would have enough fiducial markers one would still be able to reconstruct high-resolution information in the tomograms. However, our experiments where we tracked the radiation-induced motion of individual DNA-origami particles throughout the tilt series show that also the macromolecular complexes of interest move during the tilt series acquisition. We applied an overall

dose of 70 $e^-/Å^2$, and observed average radiation-induced translations of ~6 Å and radiation-induced rotations of several degrees. This movement will break the basic assumption of the tomographic reconstruction, and will limit the high-resolution information content of the tomogram.

Because correction of radiation-induced motion from one tilted image to the next would be difficult, we sought to reduce this motion experimentally by the use of ultra-stable gold grids. Using single-particle movie-processing approaches on ribosomes and apoferritin, these grids were observed to significantly reduce radiation-induced sample motion. Compared to standard copper grids with a carbon film, large specimen motions parallel to the electron beam were reduced by a factor of 50, while smaller motions perpendicular to the beam were reduced more than two-fold (Russo and Passmore, 2014). Brilot *et al* (Brilot et al., 2012) first described the large motions in the direction of the electron beam as a doming motion of the ice layer over the holes in the carbon film. Although the bulk of this motion occurs in the direction of the electron beam, the detrimental effect of this type of movement is expected to be much larger for the tilted images in the tomography experiment than for the untilted projections in single-particle analysis. Improved residuals for the fiducial alignment suggest that radiation-induced motion is indeed reduced on the gold grids. The observation that we obtained a higher resolution map from fewer sub-tomograms compared to the copper grids suggests that the reduced motion indeed resulted in tomogram reconstructions with better high-resolution information. Although the hepatitis-B sample in our experiment is basically a single-particle-like sample, we expect that the reduced radiation-induced motions on gold grids will also improve cellular tomography.

In summary, in this work we aimed to harness recent advances that have revolutionized cryo-EM single-particle analysis, i.e. regularised likelihood refinement, direct electron detection, and ultrastable gold grids, to improve 3D structure determination by sub-tomogram averaging. Using simplified test samples, we show that full CTF phase and amplitude correction improves sub-tomogram averaging, that radiation-induced motions during tilt series acquisition may be a limiting factor, and that data collection on gold grids significantly improves resolution in sub-tomogram averaging. Although the resolution we obtain from sub-tomogram averaging does not yet rival the resolution that is possible by the single-particle approach, this study is a step forward and contributes to our understanding of the remaining issues in the tomographic approach.

Experimental Procedures

Sample preparation: HBV protein and DNA origami molecules were purified as described previously (Bai et al., 2012; Wynne et al., 1999). In each case, the purified sample was mixed with 10 nm gold beads conjugated to protein-A (CMC, Utrecht) and applied to freshly plasma-cleaned holey grids (200 mesh Cu/Rh carbon support grids, or 400 mesh gold grids). Grids with the applied mixture were blotted using Whatman 1 filter paper and plunge frozen in liquid ethane using a Vitrobot (FEI) and stored in liquid nitrogen until further investigation.

Cryo-electron tomography: Vitrified samples were imaged using a FEI Titan Krios microscope operated in EFTEM mode at 300 keV extraction voltage with a 70 μm C2 aperture and a 70 μm objective aperture. Cryo-ET data was collected using SerialEM

(Mastronarde, 2005) on a K2 summit direct electron detector fitted behind an energy filter (Gatan Quantum) at a nominal magnification of 53,000x with a calibrated pixel size of 2.17 Å. The K2 summit camera was operated in counting mode at a dose rate of ~5-8 electrons/pixel/second on the camera except for the pre-illuminated images (in Figure 3A) where super-resolution mode was used. Each tilt image was divided into image frames with a ~0.5 $e^-/Å^2$ electron dose and aligned during the acquisition itself using the "Combined Filter" in the Gatan Digital Micrograph software. In tilt series where the alignment of the frames became unreliable due to increased noise due to ice thickness, the dose fractionation option was not used. For the HBV capsid sample, tilt series data were collected between ±60° with 3° tilt increments. Data were collected at 2-5 μm underfocus with a cumulative dose of 60 $e^-/Å^2$ equally fractionated over the tilt series. For DNA origami molecules, data were collected between ±30° with 5° tilt increments. A defocus of -7 μm and a cumulative electron dose of 70 $e^-/Å^2$ was applied, and was equally fractionated over each tilt angle in the series.

Fiducials in tilt series data were tracked automatically using IMOD (Kremer et al., 1996) and then inspected manually for errors. Corrections of tracking errors were made manually within IMOD, and the final aligned tilt series were produced in IMOD. Only in the comparison with strip-based CTF, the aligned tilt series data were CTF corrected by phase-flipping in IMOD. Tomogram reconstructions from the aligned tilt series were conducted using weighted-back projection implemented in Tomo3D (Agulleiro and Fernandez, 2011). All sub-tomogram averaging and single-particle analysis refinements were performed in RELION. Additional details are provided in the approach section.

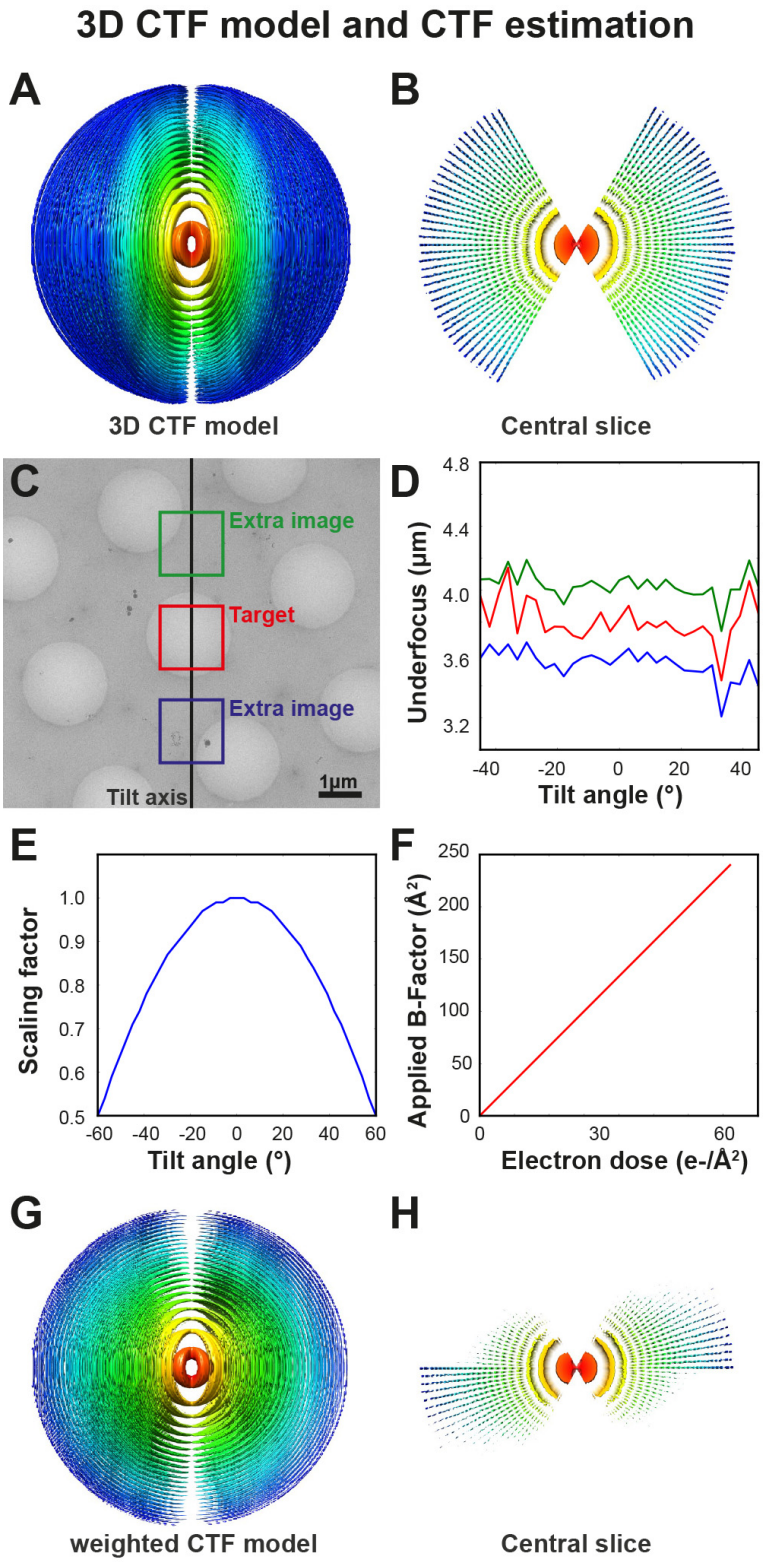

Figure 1. 3D CTF model and CTF estimation.
(A) An isosurface view of the 3D CTF model used. The volume has been pseudo-coloured based on radius (or resolution in Fourier space). Red indicates low-

resolution while blue indicates high-resolution. The 3D CTF model is made of a series of 2D slices that represent 2D CTFs of each image of the tilt series. (B) An orthogonal view of A with only the central slice shown. (C) A low-magnification picture showing the extended tilt series acquisition used in this study. Two additional images were acquired to estimate the CTF parameters in the target region of interest . (D) A plot of estimated defoci in each of the three regions shown in C at different tilt angles. (E) Tilt angle dependent scaling factor applied to weight the 3D CTF model. The multiplicative factor is equal to the cosine of the tilt angle, and scales the entire CTF curve down. (F) Dose-dependent B-factor applied to the CTF model. The slope of the linear curve was determined empirically from a previous single-particle analysis report (Scheres, 2014). (G-H) Two views of the final weighted 3D CTF model.

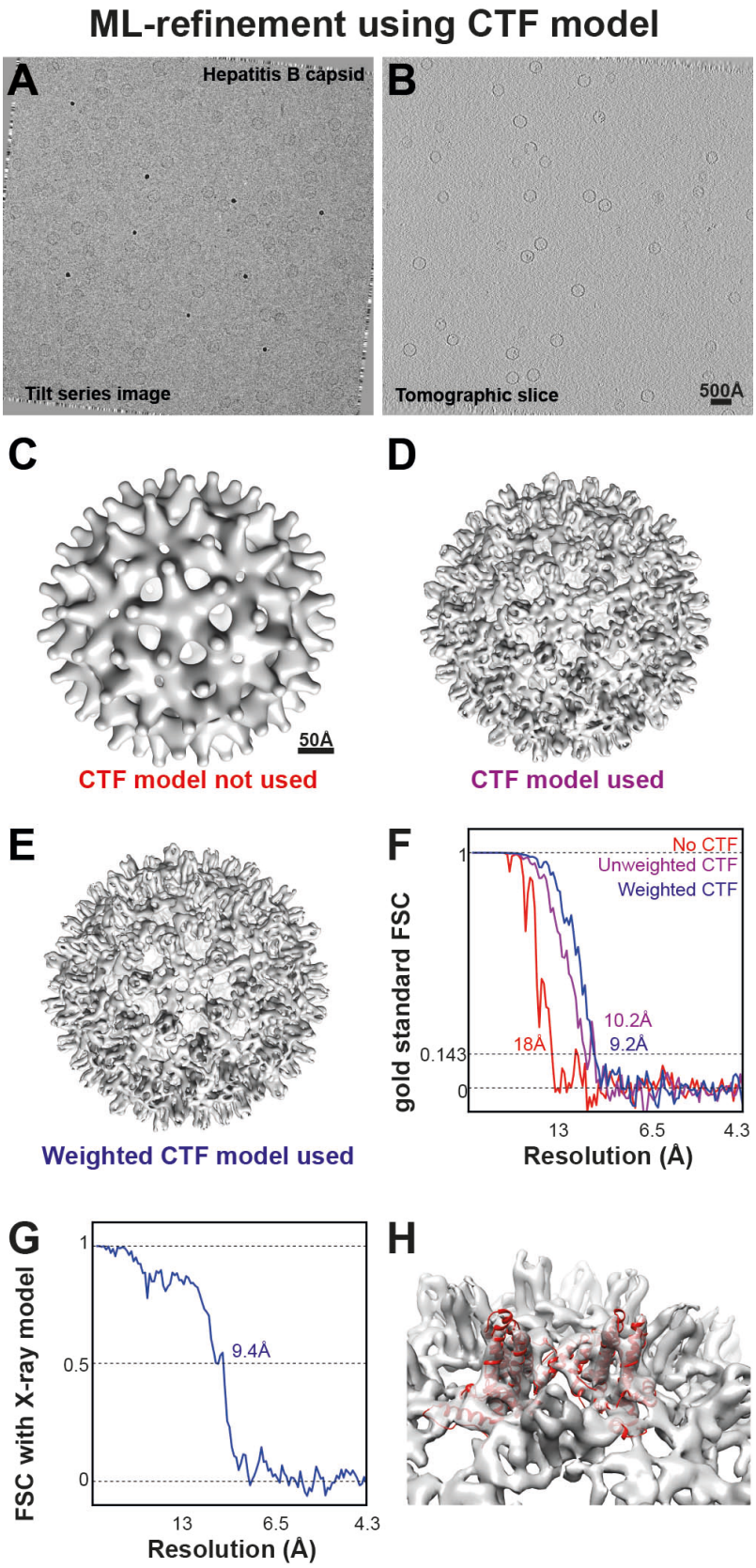

Figure 2. Maximum-Likelihood refinement using the 3D CTF model.
(A) A representative image from a tilt series of the Hepatitis B capsid sample. (B) Slice from a tomogram reconstructed from the tilt series data. (C) Isosurface

representation of the final volume of the refinement with the CTF model not used. (D) Result of refinement with the unweighted CTF model used. (E) Weighted CTF model used. (F) FSC curves showing the estimated resolution from the refinements (The same 1851 HBV particles were used in all refinements). (G) FSC curve of the best model (from the refinement with weighted CTF model) against the X-ray structure. (G) The X-ray structure is shown fitted into the sub-tomogram averaging map and secondary structure elements are clearly resolved.

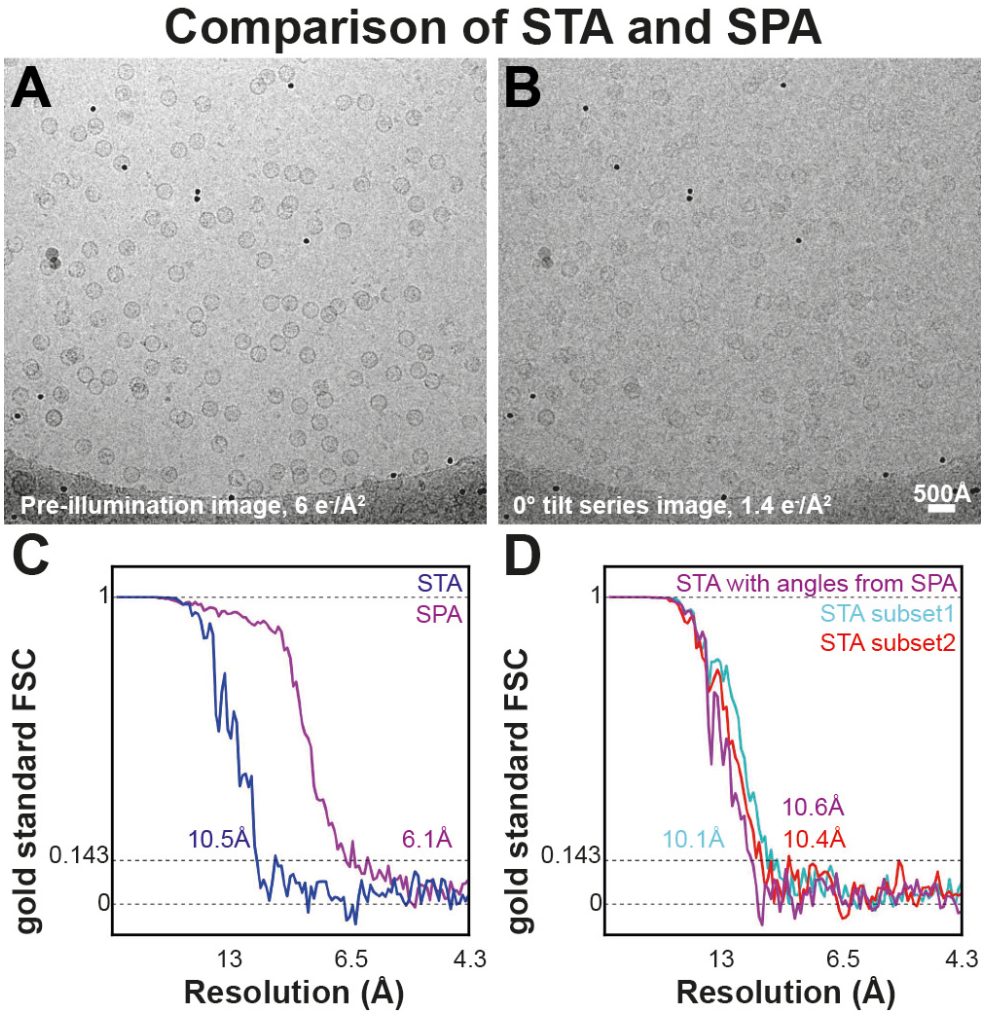

Figure 3. Pre-illumination for comparing sub-tomogram averaging (STA) and single-particle analysis (SPA).
(A) The sample was pre-illuminated with a dose of 6 $e^-/Å^2$ to record an image for single-particle analysis. (B) Immediately after this, a tilt series was collected of the same region with the same microscope parameters. (C) Sub-tomogram averaging was conducted from the tomographic data, and single-particle analysis was conducted from the pre-illumination image. FSC curves of these refinements are shown (the same 1501 HBV particles in both refinements). (D) Sub-tomogram averaging refinement of half of the particles (751 particles) that had the most similar alignment parameters in both refinements (denoted as subset1, also see Figure S4) were compared to the other half (subset2, 750 particles) that had the most different alignment parameters. There was no significant difference between the resolutions obtained in both refinements. Furthermore, applying Euler angles obtained from single-particle analysis to the entire dataset (of 1501 particles) did not lead to an improvement in sub-tomogram averaging (purple curve).

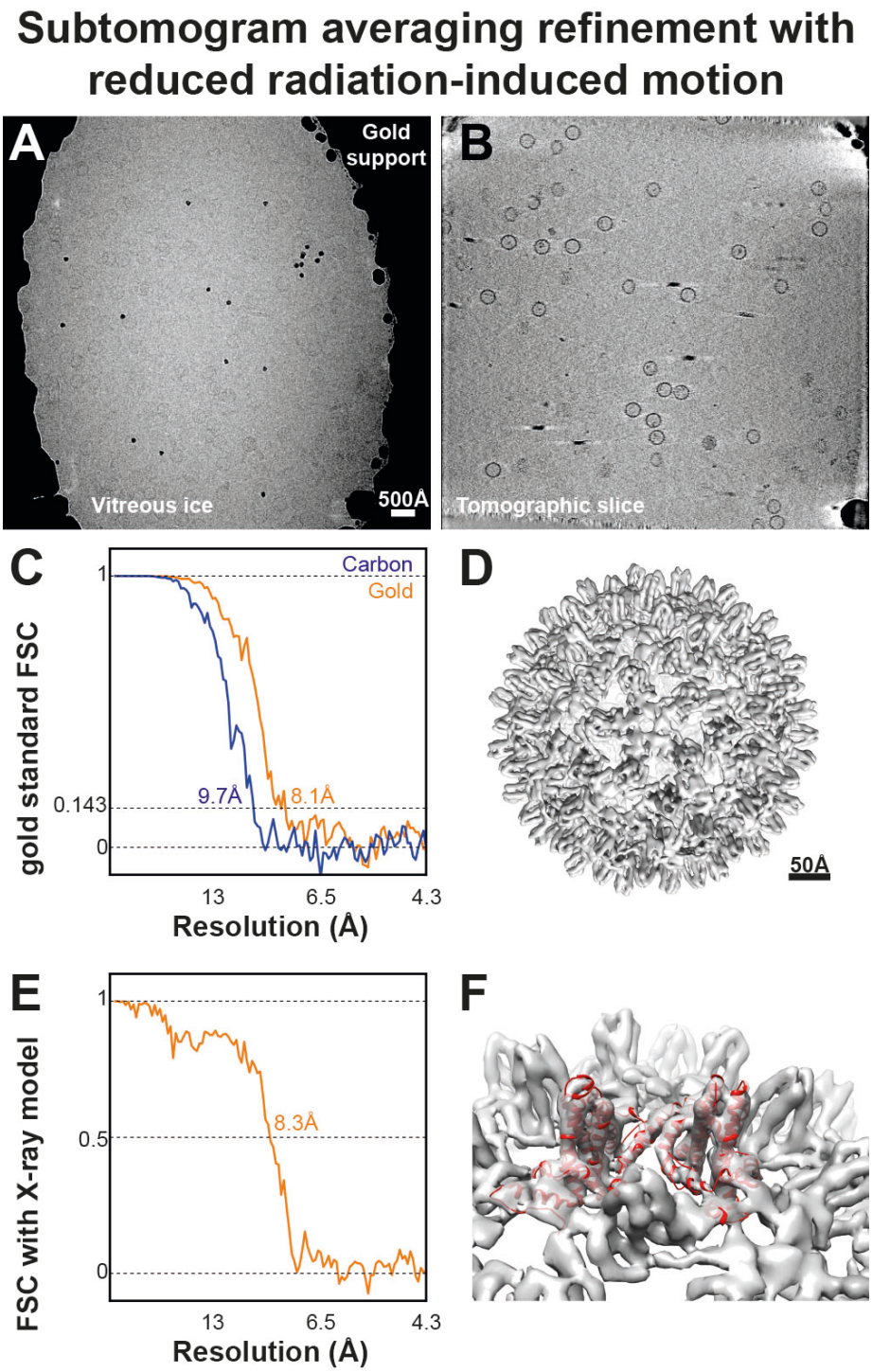

Figure 4. Sub-tomogram averaging with reduced radiation-induced motion. (A) A representative image from a tilt series of the Hepatitis B capsid sample imaged on a gold support grid. The support is seen as a high-intensity feature. (B) Slice from a tomogram reconstructed from the tilt series data. (C) FSC curves showing the estimated resolution from the refinements conducted on carbon grids and on gold grids (1145 HBV capsid particles used in both refinements). (D) Isosurface representation of the output volume from the refinement with data collected on gold grids. (E) FSC curve of the sub-tomogram averaging model from the refinement with data collected on gold grids against the X-ray structure. (G) The X-ray structure is

shown fitted into the sub-tomogram averaging map where secondary structure elements are clearly resolved.

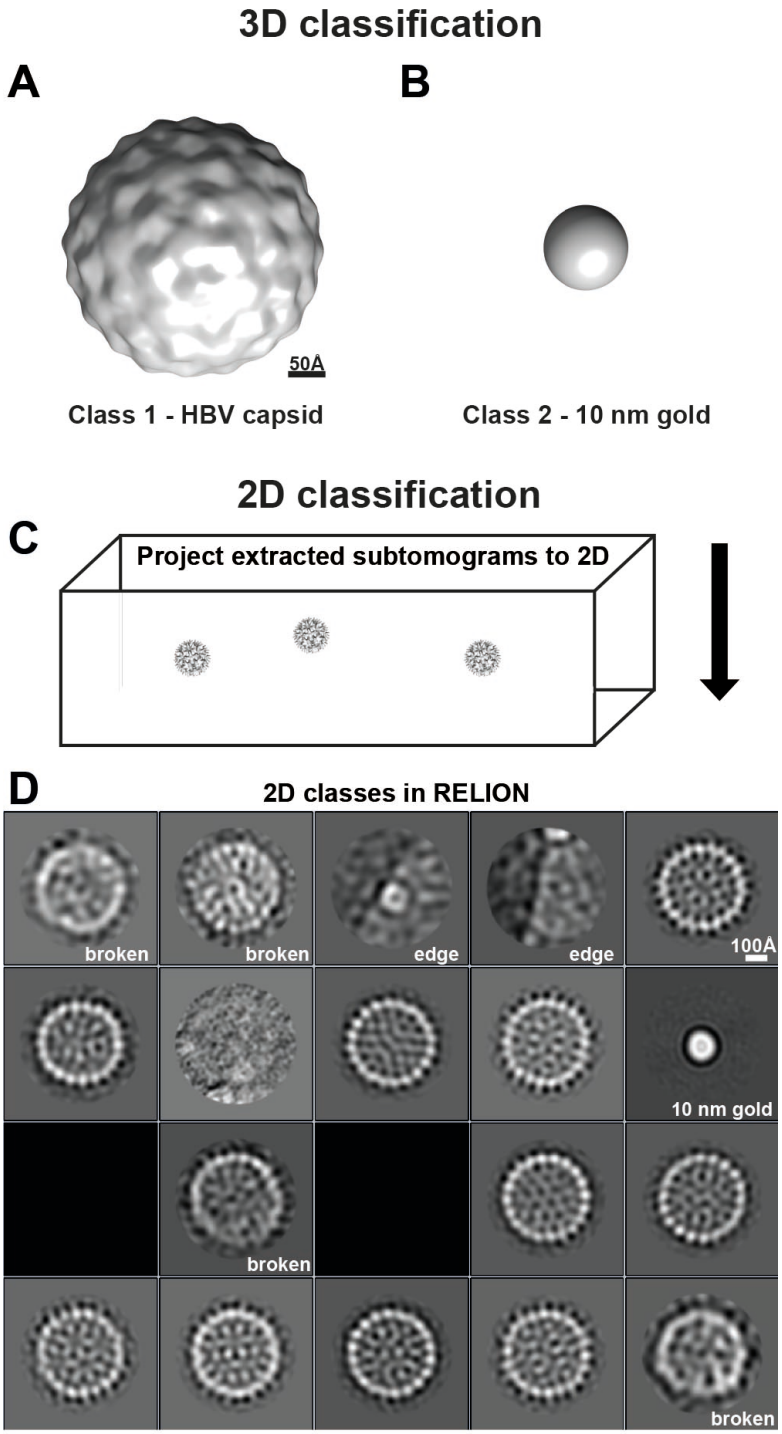

Figure S1. Initial classification of the data.
(A-B) Reference-free 3D classification of the data set was conducted. The classification clearly distinguished between extracted 10 nm gold fiducials and *bona fide* HBV capsid particles. This is a fast and easy way to remove unwanted data. (C) As an independent approach to classification, rather than extracting a 3D sub-tomogram, we extracted a 2D projection of each sub-tomogram. (D) These 2D projections were used to classify the data in a computationally economic manner

showing clearly classes corresponding to good HBV capsids. Classes with broken HBV capsids, and classes that did not correspond to HBV capsids are marked.

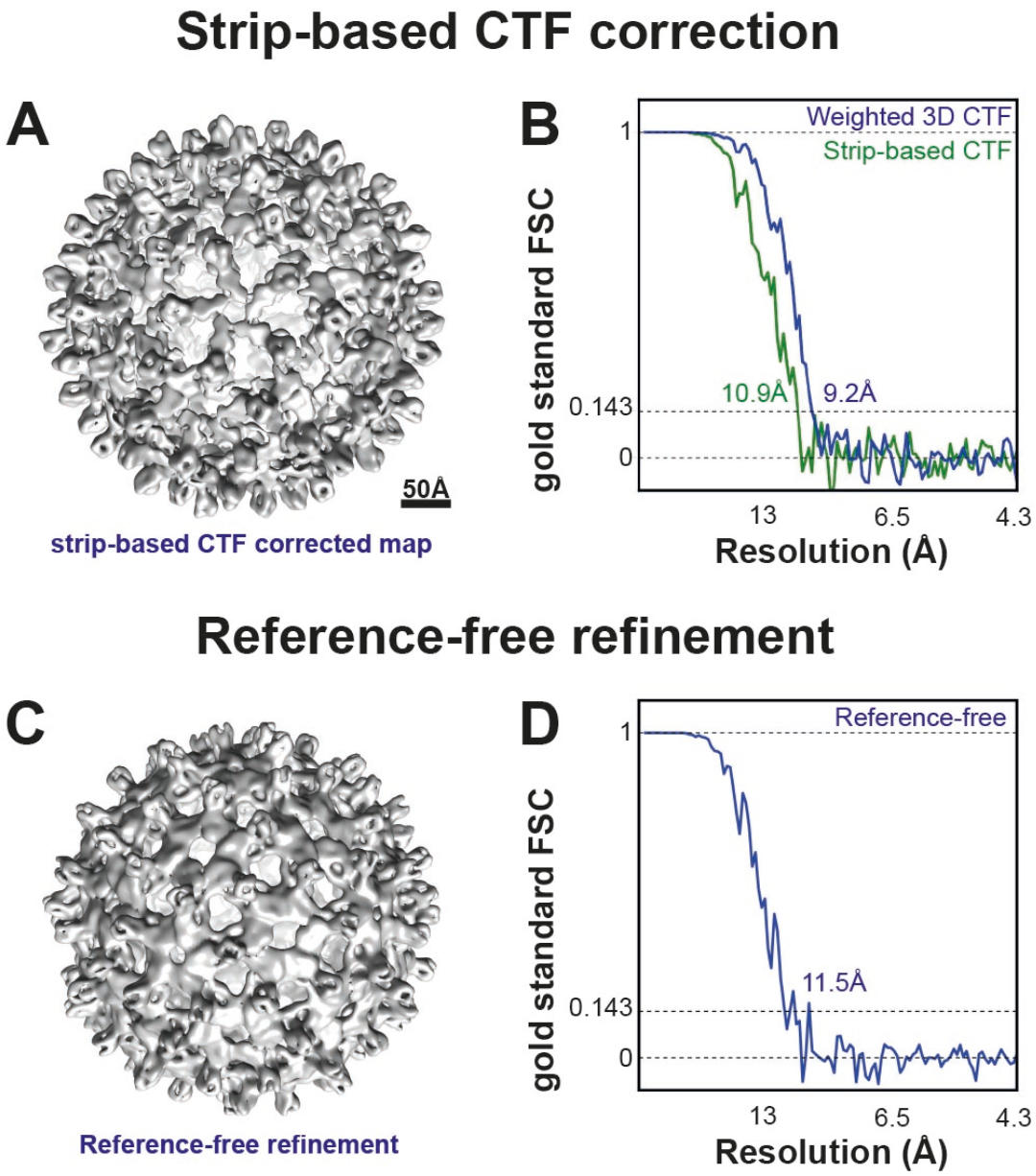

Figure S2. Strip-based CTF correction and reference-free refinements.
(A) Using conventional strip-based CTF correction implemented in IMOD, automatic refinement in RELION yielded a 10.9 Å map. Only phase-flipping and no amplitude weighting was conducted in this CTF correction. (B) Compared to the refinement using our new 3D CTF model, the resolution obtained was lower. (C) Reference-free refinements could be conducted using the same data as shown in figure 2. (D) The resolution of the output, refined structure (11.5 Å) was not as high as in cases when a reference was used (9.2 Å).

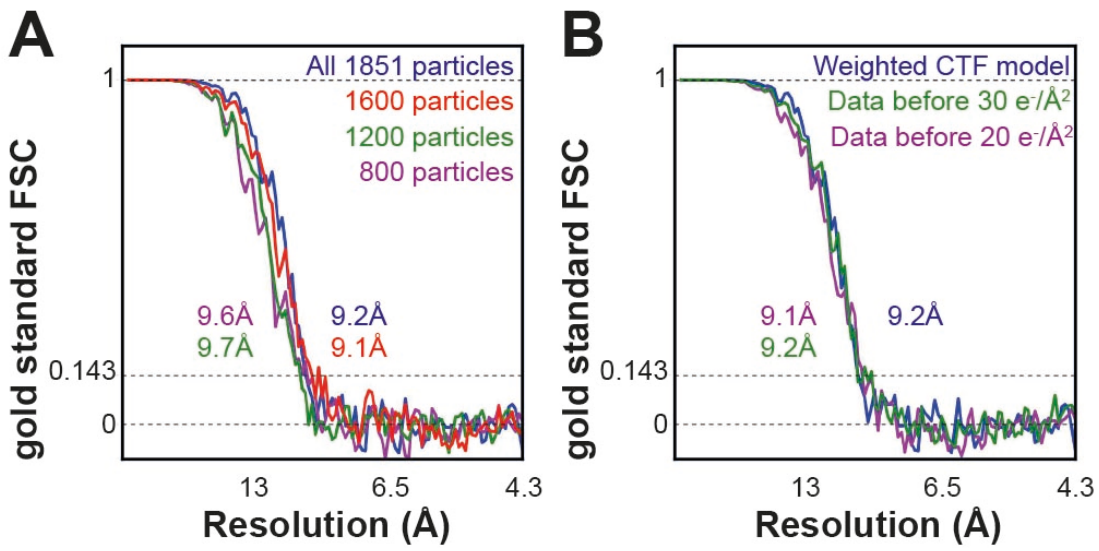

Figure S3. Resolution of sub-tomogram averaging reconstruction could not be improved by adding more data or removing subsets of the data.
(A) Different sub-tomogram averaging refinements were conducted using random subsets of the data of different sizes. A similar resolution was obtained with less particles showing that the refinement was not limited by the size of the data set. (B) Part of the data that had suffered a cumulative electron dose of 20 or 30 $e^-/Å^2$ was removed using the 3D CTF model. Compared to the full data set in which 60 $e^-/Å^2$ had been applied to the specimen, no improvement was observed (the weighted 3D CTF model was used in all refinements).

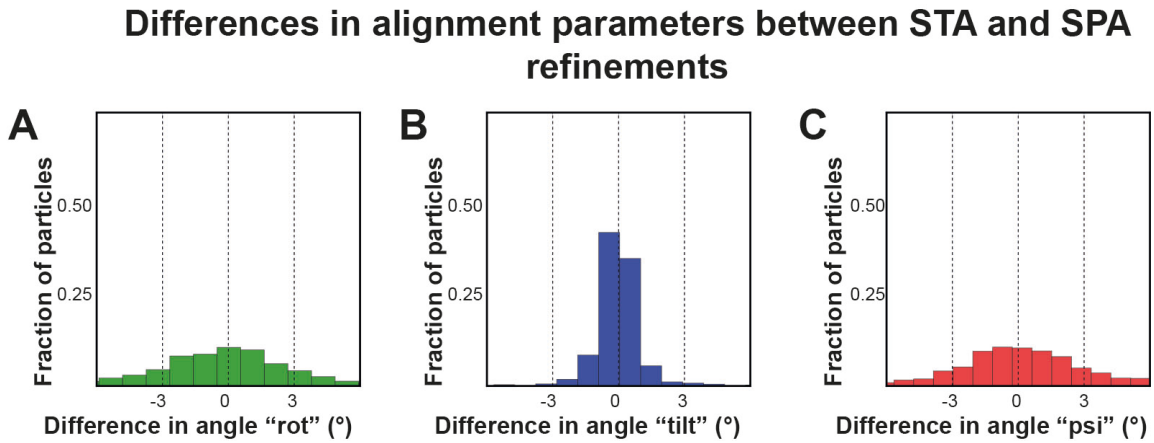

Figure S4. Histogram of differences in alignment parameters between the sub-tomogram averaging and single-particle analysis refinements.
(A) A histogram of differences of the assigned first Euler angle ("rot" in RELION) between the sub-tomogram averaging and single-particle analysis refinements presented in Figure 3. (B) Corresponding histogram for the second Euler angle "tilt". (C) Corresponding histogram for the third Euler angle "psi".

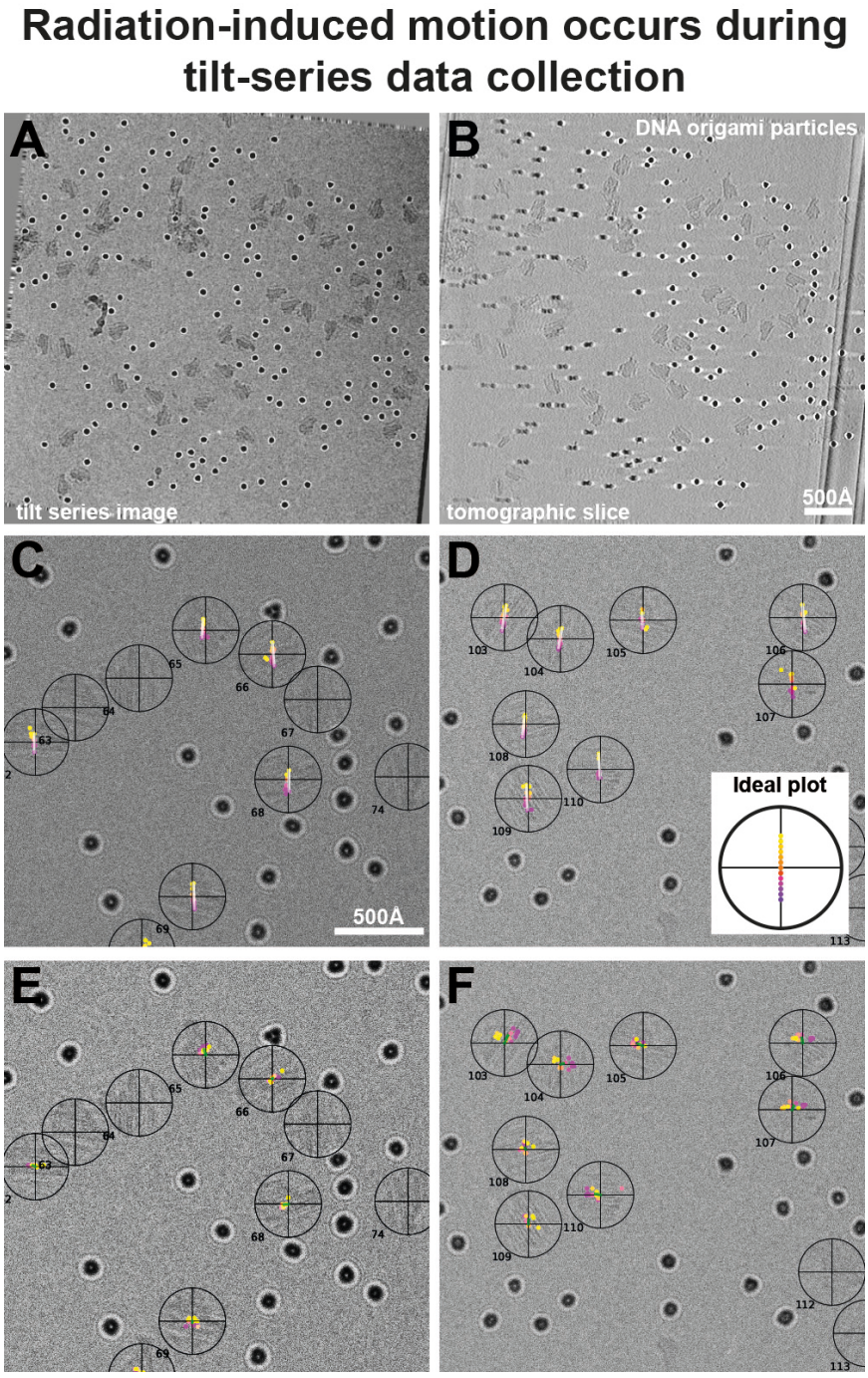

Figure S5. Radiation-induced motion occurs during tilt series data collection.
(A) A representative image from a tilt series of DNA origami molecules. Particles are large and asymmetric, allowing accurate assignment of orientation angles. (B) Slice from a tomogram reconstructed from the tilt series data. (C-D) Euler angles from sub-tomogram averaging were assumed to be correct and a tilt-pair like analysis was conducted for each particle. The grid was tilted at defined increments during tilt series data collection. If there were no radiation-induced motion, then the plot would resemble the schematic shown in the inset of D. However, significant deviations from ideality were observed. Only particles where the plotted points were roughly on a line (white lines) were used to measure differences in Euler angles to prevent

quantification of mis-aligned particles. (E-F) Averaged Δx, Δy shifts between the selected sub-tomogram averaging alignment parameters and the single-particle analysis alignment parameters plotted onto the zero degree image of the tilt series, scaled by multiplying each shift by five (the two images shown are from different tilt series). A green line is drawn to illustrate the average shift.

Difference between the actual and expected positions of fiducial marker beads in tilted images

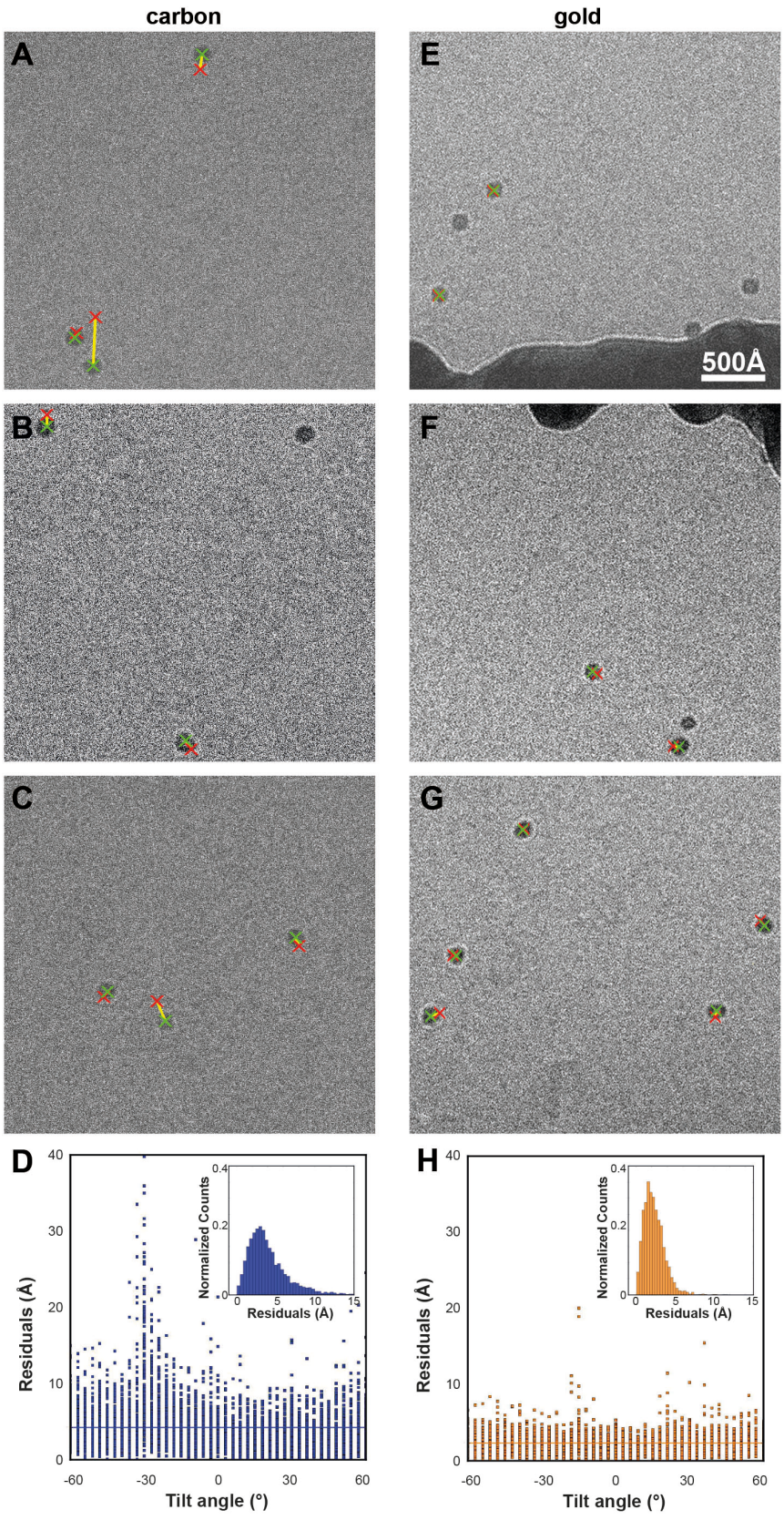

Figure S6. Radiation-induced movement of fiducial markers is reduced on gold grids.
(A-C) Three examples of the actual positions of 10 nm gold fiducial markers (green cross) and their expected positions (red cross) in 60° tilted images of tilt series collected on ordinary carbon support grids have been shown in an IMOD residual plot. Plotted positions for the same gold fiducial marker are connected with a yellow line. (D) The overall average residual over 15 tilt series (total 5452 residuals) collected on carbon support grids was 4.3 Å (horizontal blue line). Inset: histogram of residuals on carbon support grids. (E-G) Three examples of the corresponding plot for data collected on gold grids. (H) The overall averaged residual over 11 tilt series (total 3344 residuals) collected on gold support grids was 2.3 Å (orange line). Inset: histogram of residuals on gold support grids.

References:

Agulleiro, J.I., and Fernandez, J.J. (2011). Fast tomographic reconstruction on multicore computers. Bioinformatics *27*, 582-583.

Allegretti, M., Mills, D.J., McMullan, G., Kuhlbrandt, W., and Vonck, J. (2014). Atomic model of the F420-reducing [NiFe] hydrogenase by electron cryo-microscopy using a direct electron detector. Elife *3*, e01963.

Bai, X.C., Fernandez, I.S., McMullan, G., and Scheres, S.H. (2013). Ribosome structures to near-atomic resolution from thirty thousand cryo-EM particles. Elife *2*, e00461.

Bai, X.C., Martin, T.G., Scheres, S.H., and Dietz, H. (2012). Cryo-EM structure of a 3D DNA-origami object. Proc Natl Acad Sci U S A *109*, 20012-20017.

Bai, X.C., McMullan, G., and Scheres, S.H. (2015). How cryo-EM is revolutionizing structural biology. Trends Biochem Sci *40*, 49-57.

Bartesaghi, A., Lecumberry, F., Sapiro, G., and Subramaniam, S. (2012). Protein secondary structure determination by constrained single-particle cryo-electron tomography. Structure *20*, 2003-2013.

Bartesaghi, A., Matthies, D., Banerjee, S., Merk, A., and Subramaniam, S. (2014). Structure of beta-galactosidase at 3.2-A resolution obtained by cryo-electron microscopy. Proc Natl Acad Sci U S A *111*, 11709-11714.

Bartesaghi, A., and Subramaniam, S. (2009). Membrane protein structure determination using cryo-electron tomography and 3D image averaging. Curr Opin Struct Biol *19*, 402-407.

Baumeister, W. (2002). Electron tomography: towards visualizing the molecular organization of the cytoplasm. Curr Opin Struct Biol *12*, 679-684.

Beck, M., Lucić, V., Förster, F., Baumeister, W., and Medalia, O. (2007). Snapshots of nuclear pore complexes in action captured by cryo-electron tomography. Nature *449*, 611-615.

Bharat, T.A., Castillo Menendez, L.R., Hagen, W.J., Lux, V., Igonet, S., Schorb, M., Schur, F.K., Krausslich, H.G., and Briggs, J.A. (2014). Cryo-electron microscopy of tubular arrays of HIV-1 Gag resolves structures essential for immature virus assembly. Proc Natl Acad Sci U S A *111*, 8233-8238.

Bharat, T.A., Davey, N.E., Ulbrich, P., Riches, J.D., de Marco, A., Rumlova, M., Sachse, C., Ruml, T., and Briggs, J.A. (2012). Structure of the immature retroviral capsid at 8 Å resolution by cryo-electron microscopy. Nature *487*, 385-389.

Bharat, T.A., Riches, J.D., Kolesnikova, L., Welsch, S., Krahling, V., Davey, N., Parsy, M.L., Becker, S., and Briggs, J.A. (2011). Cryo-electron tomography of Marburg virus particles and their morphogenesis within infected cells. PLoS Biol *9*, e1001196.

Briggs, J.A. (2013). Structural biology in situ--the potential of subtomogram averaging. Curr Opin Struct Biol *23*, 261-267.

Briggs, J.A., Riches, J.D., Glass, B., Bartonova, V., Zanetti, G., and Kräusslich, H.G. (2009). Structure and assembly of immature HIV. Proc Natl Acad Sci U S A *106*, 11090-11095.

Brilot, A.F., Chen, J.Z., Cheng, A., Pan, J., Harrison, S.C., Potter, C.S., Carragher, B., Henderson, R., and Grigorieff, N. (2012). Beam-induced motion of vitrified specimen on holey carbon film. J Struct Biol *177*, 630-637.

Campbell, M.G., Cheng, A., Brilot, A.F., Moeller, A., Lyumkis, D., Veesler, D., Pan, J., Harrison, S.C., Potter, C.S., Carragher, B.*, et al.* (2012). Movies of ice-embedded particles enhance resolution in electron cryo-microscopy. Structure *20*, 1823-1828.
Chen, S., McMullan, G., Faruqi, A.R., Murshudov, G.N., Short, J.M., Scheres, S.H., and Henderson, R. (2013). High-resolution noise substitution to measure overfitting and validate resolution in 3D structure determination by single particle electron cryomicroscopy. Ultramicroscopy *135*, 24-35.
Dempster, A.P., Laird, N.M., and Rubin, D.B. (1977). Maximum likelihood from incomplete data via the EM algorithm. Journal of the Royal Statistical Society, Series B *39*, 1-38.
Downing, K.H. (1988). Observations of restricted beam-induced specimen motion with small-spot illumination. Ultramicroscopy *24*, 387-397.
Eibauer, M., Hoffmann, C., Plitzko, J.M., Baumeister, W., Nickell, S., and Engelhardt, H. (2012). Unraveling the structure of membrane proteins in situ by transfer function corrected cryo-electron tomography. J Struct Biol *180*, 488-496.
Förster, F., Medalia, O., Zauberman, N., Baumeister, W., and Fass, D. (2005). Retrovirus envelope protein complex structure in situ studied by cryo-electron tomography. Proc Natl Acad Sci U S A *102*, 4729-4734.
Fromm, S.A., Bharat, T.A., Jakobi, A.J., Hagen, W.J., and Sachse, C. (2014). Seeing tobacco mosaic virus through direct electron detectors. J Struct Biol.
Grünewald, K., Desai, P., Winkler, D.C., Heymann, J.B., Belnap, D.M., Baumeister, W., and Steven, A.C. (2003). Three-dimensional structure of herpes simplex virus from cryo-electron tomography. Science *302*, 1396-1398.
Henderson, R., and Glaeser, R.M. (1985). Quantitative analysis of image contrast in electron micrographs of beam-sensitive crystals. Ultramicroscopy *16*, 139-150.
Kremer, J.R., Mastronarde, D.N., and McIntosh, J.R. (1996). Computer visualization of three-dimensional image data using IMOD. J Struct Biol *116*, 71-76.
Li, X., Mooney, P., Zheng, S., Booth, C.R., Braunfeld, M.B., Gubbens, S., Agard, D.A., and Cheng, Y. (2013). Electron counting and beam-induced motion correction enable near-atomic-resolution single-particle cryo-EM. Nature methods *10*, 584-590.
Liao, M., Cao, E., Julius, D., and Cheng, Y. (2013). Structure of the TRPV1 ion channel determined by electron cryo-microscopy. Nature *504*, 107-112.
Lin, J., Okada, K., Raytchev, M., Smith, M.C., and Nicastro, D. (2014). Structural mechanism of the dynein power stroke. Nat Cell Biol *16*, 479-485.
Mastronarde, D.N. (2005). Automated electron microscope tomography using robust prediction of specimen movements. J Struct Biol *152*, 36-51.
McMullan, G., Faruqi, A.R., Clare, D., and Henderson, R. (2014). Comparison of optimal performance at 300 keV of three direct electron detectors for use in low dose electron microscopy, Vol 1406.
McMullan, G., Faruqi, A.R., Henderson, R., Guerrini, N., Turchetta, R., Jacobs, A., and van Hoften, G. (2009). Experimental observation of the improvement in MTF from backthinning a CMOS direct electron detector. Ultramicroscopy *109*, 1144-1147.
Mindell, J.A., and Grigorieff, N. (2003). Accurate determination of local defocus and specimen tilt in electron microscopy. J Struct Biol *142*, 334-347.
Rosenthal, P.B., and Henderson, R. (2003). Optimal determination of particle orientation, absolute hand, and contrast loss in single-particle electron cryomicroscopy. J Mol Biol *333*, 721-745.

Rubinstein, J.L., and Brubaker, M.A. (2014). Alignment of cryo-EM movies of individual particles by optimization of image translations. In ArXiv e-prints\, pp. 6789\.
Russo, C.J., and Passmore, L.A. (2014). Electron microscopy. Ultrastable gold substrates for electron cryomicroscopy. Science *346*, 1377-1380.
Scheres, S.H. (2012a). A Bayesian view on cryo-EM structure determination. J Mol Biol *415*, 406-418.
Scheres, S.H. (2012b). RELION: implementation of a Bayesian approach to cryo-EM structure determination. J Struct Biol *180*, 519-530.
Scheres, S.H. (2014). Beam-induced motion correction for sub-megadalton cryo-EM particles. Elife *3*, e03665.
Scheres, S.H., and Chen, S. (2012). Prevention of overfitting in cryo-EM structure determination. Nature methods *9*, 853-854.
Schur, F.K., Hagen, W.J., Rumlova, M., Ruml, T., Muller, B., Krausslich, H.G., and Briggs, J.A. (2014). Structure of the immature HIV-1 capsid in intact virus particles at 8.8 A resolution. Nature.
Subramaniam, S. (2013). Structure of trimeric HIV-1 envelope glycoproteins. Proc Natl Acad Sci U S A *110*, E4172-4174.
Tocheva, E.I., Matson, E.G., Morris, D.M., Moussavi, F., Leadbetter, J.R., and Jensen, G.J. (2011). Peptidoglycan remodeling and conversion of an inner membrane into an outer membrane during sporulation. Cell *146*, 799-812.
Wong, W., Bai, X.C., Brown, A., Fernandez, I.S., Hanssen, E., Condron, M., Tan, Y.H., Baum, J., and Scheres, S.H. (2014). Cryo-EM structure of the Plasmodium falciparum 80S ribosome bound to the anti-protozoan drug emetine. Elife *3*.
Wright, E.R., Iancu, C.V., Tivol, W.F., and Jensen, G.J. (2006). Observations on the behavior of vitreous ice at approximately 82 and approximately 12 K. J Struct Biol *153*, 241-252.
Wynne, S.A., Crowther, R.A., and Leslie, A.G. (1999). The crystal structure of the human hepatitis B virus capsid. Mol Cell *3*, 771-780.